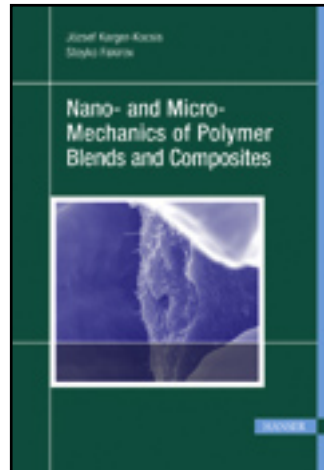


HANSER



### Sample Pages

Nano- and Micromechanics of Polymer Blends and Composites

Herausgegeben von József Karger-Kocsis, Stoyko Fakirov

ISBN: 978-3-446-41323-8

For further information and order see

<http://www.hanser.de/978-3-446-41323-8>  
or contact your bookseller.

higher filler-polymer interaction ( $-\varepsilon/k_B T$ ), the chain segments located at the interphase possess non-equilibrium structure due to the fact that their relaxation times reach a value many orders of magnitude higher compared to the unperturbed bulk under given conditions (the ergodicity is broken within the interphase).

The effect of perturbed segmental dynamics within the interphase is, most probably, responsible for the phenomenon presented in Figure 6.6, where the temperature dependence of the relative storage modulus,  $G'_r$ , of entangled and cross-linked matrix nanocomposite above  $T_g$  is presented. It is evident that the reinforcement displays temperature dependence proportional to the nature of the polymer network. As temperature increases, the segmental mobility of the interphase chains is continuously released resulting in a slow decrease of the interphase stiffness. Whilst the neat entangled network of poly(vinyl acetate) (PVAc) loses its elasticity with the increasing temperature due to the normal mode relaxation processes, the neat cross-linked poly(ethyl acrylate) elastomer slightly stiffens in accordance with the rubber elasticity theory. Hence, relating nanocomposite elastic modulus to that of neat matrix leads to either positive or negative slope of the temperature dependence,  $G'_r$ - $T$  dependence in Figure 6.6. Moreover, substantial effect of matrix-filler bonding can be recognized. In the case of covalent filler-matrix bonding, the mobility release is substantially slower

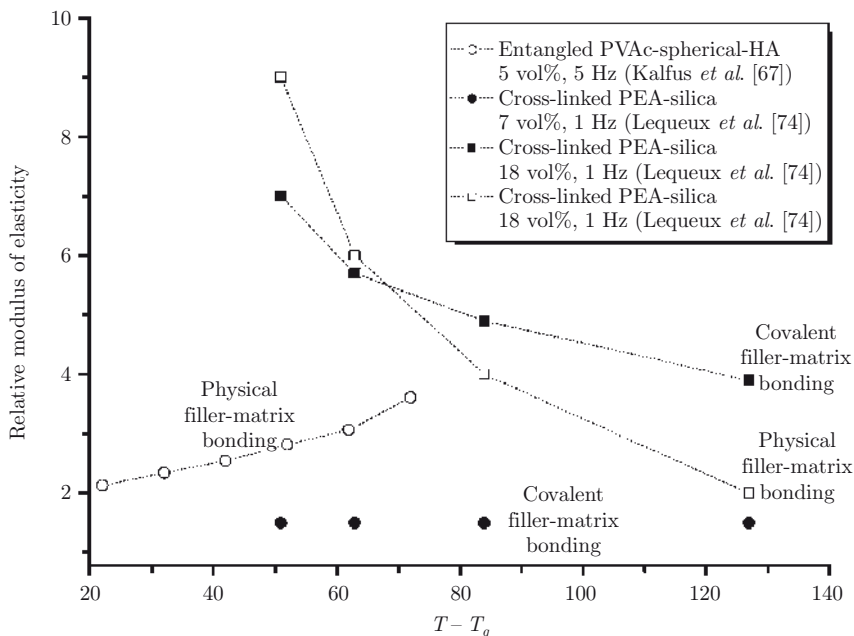


**Figure 6.6.** Temperature dependence of relative modulus of elasticity of an entangled and cross-linked nanocomposite

with increasing temperature compared to the system, where physical interaction between filler and matrix is dominating.

### 6.5. Strain induced softening of amorphous polymer nanocomposites

The strain induced softening of both entangled and cross-linked nanocomposites above their  $T_g$ , commonly termed the Payne effect [76], is a very important part of nanocomposite physics. Currently, it is in the center of interest of many researchers due to its principal relevance for the determination of a physically correct theory of nano-reinforcing mechanisms. First, it is necessary to emphasize that there is no consensus in literature on the origin of this phenomenon and, principally, two major concepts can be recognized [71,77,80]. The first concept is based on the assumption that the polymer matrix properties are modified by the filler surface corresponding to the immobilization mechanism as it has already been outlined above. During the large strain amplitudes, the chain desorption, slippage and subsequent segmental mobilization occur. Undoubtedly, this is modulated by other phenomena resulting from the structural inhomogeneity of polymer nanocomposite. The second concept utilizes the idea of filler-network structure exhibiting enough stiffness for rubbery matrix reinforcement. At high strain amplitudes, the breakage of the filler network causes partial loss of the composite stiffness. Increasing number of recently published experimental and simulation data considerably enhance validity of the first concept, which seems to be the only one able to bring a physically correct solution of the Payne effect and nanocomposite reinforcement above the matrix  $T_g$ . Nevertheless, it does not diminish the role of the inhomogeneous dispersion of filler nanoparticles. Poor dispersion of nanoparticles seems to be rather indirect by affecting local stress-strain field, accessibility of filler surface for adsorption processes, *etc.*

Schematic representation of the Payne effect for the entangled PVAc above its  $T_g$  filled with spherical and platelet hydroxyapatite nanoparticles (aspect ratio  $A_r = 10$ ) is shown in Figure 6.7. Whilst neat PVAc exhibited constant modulus up to the maximum relative strain amplitude of 15%, the nano-filled samples softened even below 1–2% strain amplitude. Thus, a remarkable difference between linear low amplitude modulus (LAM) and non-linear high amplitude modulus (HAM) can be seen. The tangent delta increased at strain amplitudes of approximately 1–15%. At first sight, the Payne effect was more pronounced for the PVAc-platelet-HA nanocomposite. On closer look, this can be attributed to the higher extent of the filler-matrix interface area and not to the filler network and cluster percolation expectable at lower  $v_f$  compared to the spherical filler. This is clearly seen in Figure 6.8, where the low and high amplitude relative storage moduli are presented in dependence on the filler-matrix contact area. Obviously, as the strain amplitude increases the interphase is more and more perturbed. To reveal the difference of the Payne effect in an entangled and cross-linked nanocomposite above  $T_g$ , the dependence of the ratio LAM/HAM on temperature for different systems is shown in Figure 6.9. The related curve has a similar dependence as that shown in Figure 6.6.

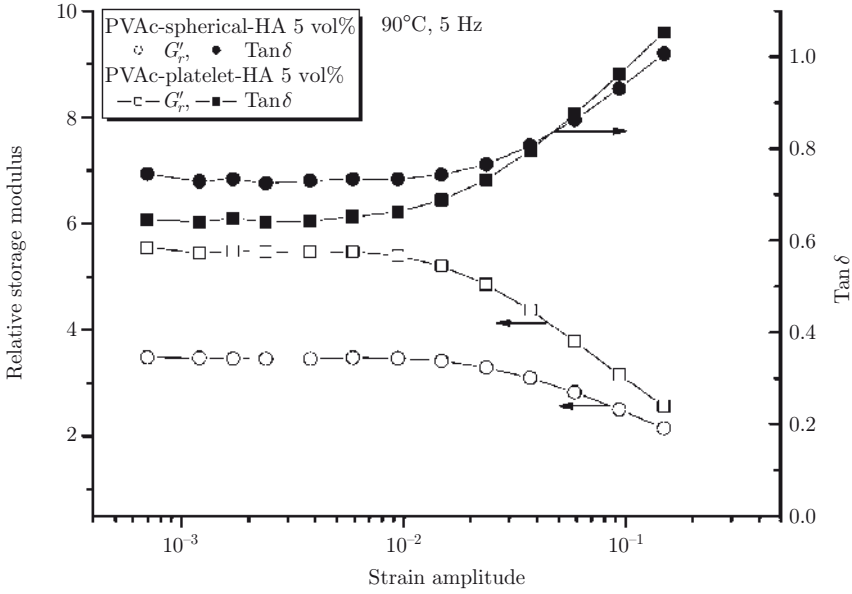


**Figure 6.7.** Example of dynamic strain softening of amorphous nanocomposite above neat matrix  $T_g$ . Hydroxyapatite spherical and platelet nanoparticles were used as filler. Experimental points were adopted from reference [79]

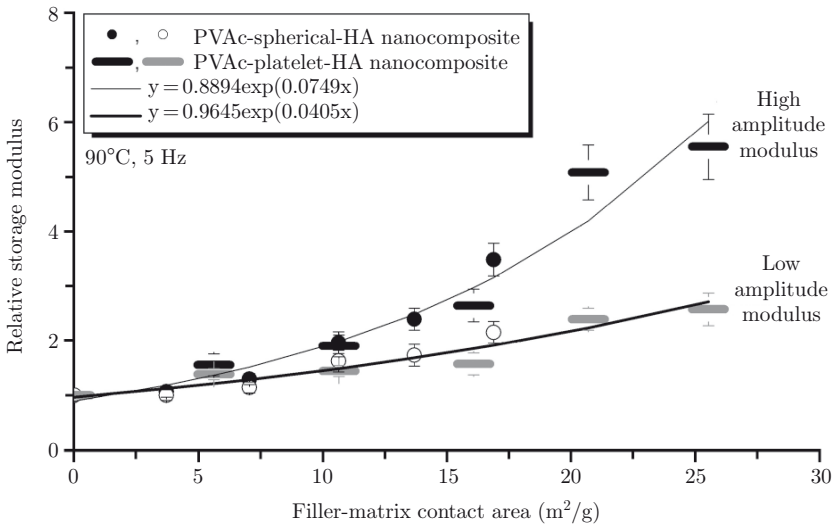


**Figure 6.8.** Effect of nanoparticle shape on the Payne effect; HAM – high amplitude modulus (non-linear) and LAM – low amplitude modulus (linear). Experimental points were adopted from reference [79]

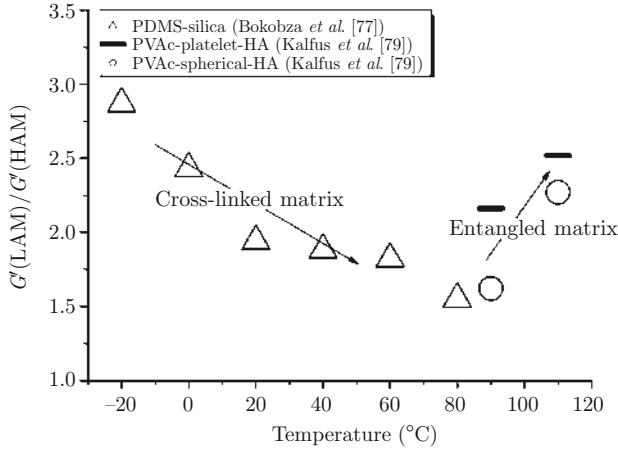


**Figure 6.9.** Temperature dependence of the LAM/HAM (low amplitude modulus/high amplitude modulus) for cross-linked polydimethyl siloxane (PMDS)-silica nanocomposite ( $v_f = 0.15$ ) and entangled PVAc-HA nanocomposite ( $v_f = 0.05$ )

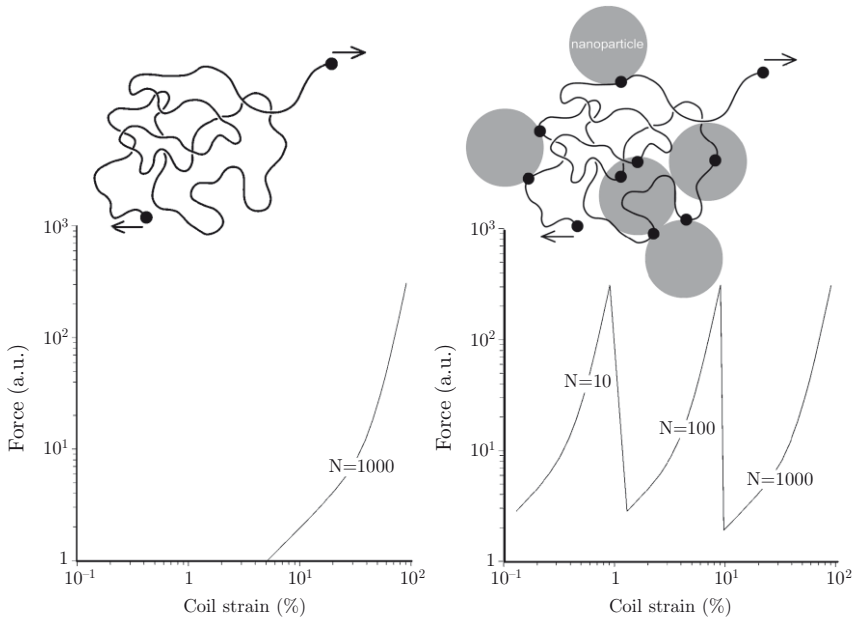


**Figure 6.10.** Sketch of force response of free random coil and adsorbed chain in dependence on the coil strain related to the maximum elongation,  $100\% \approx 0.81 Nb$ . Whilst free coil exhibits Gaussian response under given low strain approximately up to 20%, adsorbed loops and bridges, represented by  $N = 10$  and 100, are highly Langevinean with incremental stiffness considerably increased. Strain induced perturbation of interphase accompanied by desorption of trains causes significant local stress and strain relief and, consequently, a lower stiffness

**Flaws in engineering design and setup.** If one intends to eliminate the machine background from a measured pattern, it is necessary to extract the exposure intervals, primary beam intensities,  $I_0$ , and attenuated intensities,  $I_1$ , from complex data sets which are different at different beamlines. Moreover, the sequence of the stored numbers changes as a function of the wiring during setup. Thus, if background correction and normalization are not done by the beamline staff, some users will not be able to carry out these steps.

On the other hand, if there is a normalization service, the result will be written into a set of files in another proprietary data format, and it may happen that during this process data are not copied which may be essential for further data evaluation (*e.g.*, the elapsed time since the start of the experiment, which is the most important parameter in any mechanical test – cf. Figure 8.11).

Even more severe flaws are encountered. For example, the student developer of an extensometer control does not hand over the signals from the load cell and from the transducer to channels of the voltage-to-frequency (VDC) converters of the standard beamline electronics, but carries out digitization on hardware of his own with a cycle time of his own. Finally, they are stored in an ASCII file on his own computer, using his computer clock as a second time normal. As long as the cycle time is longer than 10 s, a skilled programmer will be able to modify his data pre-evaluation module in such a way that it compensates this flaw.

**Curing flaws by computer programming.** In quintessence, the consistent evaluation of streams of scattering data remains a computer programming task, and thus, programming skills are required for a successful work with multi-dimensional scattering data. Scientists providing these skills will utilize and modify open sources (see for instance [59]). Without these skills, even the few popular data evaluation programs such as Fit2D [60] will probably not be employed in an efficient manner.

**Automation – the next challenge.** In a dynamical experiment, hundreds of 2D scattering patterns are collected which must be evaluated. Thus, efficient automation is essential. Instead of writing a thoroughly planned script and running it automatically on all patterns of the series, a user merely trained to operate programs with graphical user interfaces is easily misled. Having carried out the experiment, he will use the computer in accordance with his training: Install a user-friendly evaluation program and start to click buttons without resorting to manual or theory. Operated in such a way, a user-friendly evaluation program becomes data-hostile. Moreover, the processing of voluminous data sets turns into an unmanageable task.

For instance, Fit2D is frequently used to extract slices\* from 2D scattering patterns, whereas either an azimuthal average or a projection would have been appropriate. Even such simple and inappropriate operation will turn into a nightmare, when Fit2D is operated by mouse clicks and many patterns are operated. Finally, noisy slices are extracted instead of low-noise integrated

---

\* Slices are curves that show the intensity along a straight path in the pattern.

curves. As a consequence, further processing will produce low-significance results.

### 8.5. Techniques: Dynamic vs. stretch-hold

Only a few years ago, dynamic experiments with a good signal-to-noise (S/N) ratio of the scattering patterns were not possible. Therefore many of the studies listed in this chapter have been performed by means of the older stretch-hold technique. A recent comparative study [61] unexpectedly revealed pronounced differences after switching from stretch-hold to a slow dynamic experiment. Consequently, results on the nanostructure evolution retrieved in stretch-hold studies may be used only with a lot of cautiousness to explain the dynamic loading process that is relevant in practical applications.

Figure 8.10 shows in the top row (continuous straining experiment) scattering patterns with narrow and detailed peaks, although the technique implies integration over a considerable interval of the elongation  $\varepsilon$  ( $\Delta\varepsilon \approx 0.05$ ), whereas the scattering patterns accumulated during the same beamtime in the stretch-hold technique at constant elongation appear much more blurred and show a stronger equatorial streak. Thus, this comparative experiment demonstrates that during the hold state in a stretch-hold experiment a considerable change of the nanostructure inside the composite may occur.

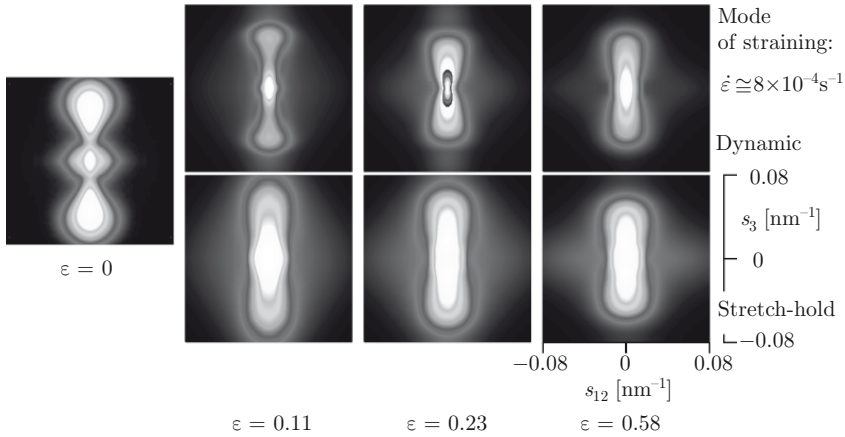


**Figure 8.10.** Comparison between SAXS patterns recorded during continuous straining (top row,  $\dot{\varepsilon} \approx 10^{-1} \text{s}^{-1}$ ) of hard-elastic PP films and results from the corresponding stretch-hold experiment (bottom row)

### 8.6. Advanced goal: Identification of mechanisms

One of the most important goals of the method is the elucidation of the mechanisms of nanostructure evolution during application of mechanical load. In the previous section it has been demonstrated that for this purpose not the

stretch-hold technique, but the recording of scattering patterns during a dynamic materials test should be applied.

Moreover, concerning the mechanical test itself, not only the classical method of continuous straining should be considered, because of the fact that during service a component\* made from a polymer nanocomposite will frequently be subjected to vibrations causing many cycles of alternating load – with materials fatigue becoming the most important reason for failure.

The scientific questions, which have recently come into reach, shall be demonstrated by results of a recent load-reversal study [62]. Figure 8.11 displays the macroscopic parameters and some of the nanostructure parameters as a function of the elapsed time. The parameters of the nanostructure have been evaluated from X-ray scattering data.

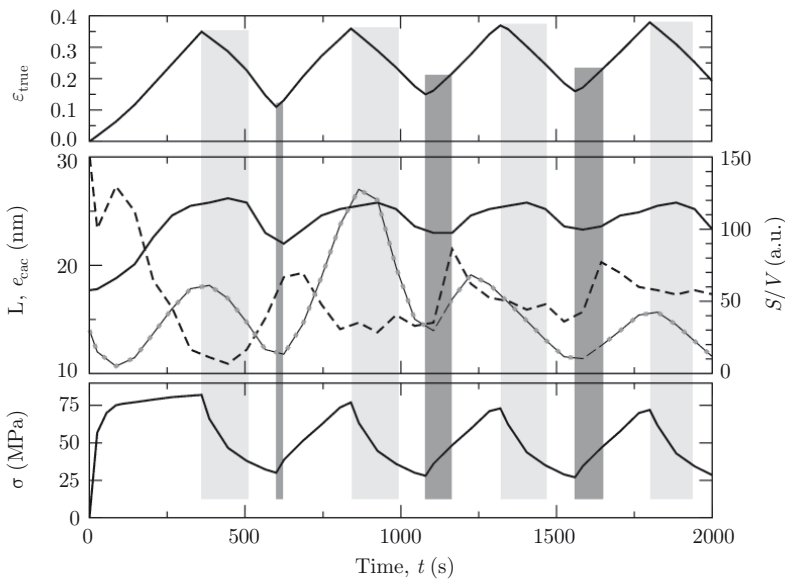


**Figure 8.11.** Dynamic load-reversal mechanical test of hard-elastic PP film. As a function of the elapsed time,  $t$ , nanostructural parameters (diagram in the middle) and the macroscopic parameters elongation,  $\varepsilon$  (top), and tensile stress,  $\sigma$  (bottom) are displayed. The middle diagram shows the long period,  $L$  (solid line), the lateral extension  $\varepsilon_{\text{cac}}$  (dashed) of the layers, and a quantity  $S/V$  (solid line with dots) which is a measure of the number of lamellae in the material. Vertical bars indicate zones of strain-induced crystallization (dark gray) and relaxation-induced melting (light gray), respectively

**Experimental.** Commercial films of uniaxially oriented, hard-elastic PP were used to punch out tensile bars (DIN 53504) which were subjected to mechanical load parallel to the direction of the preferential orientation. The thickness of the films was 50  $\mu\text{m}$ . Because of the fact that discrete X-ray scattering was observed

\* Consider, for example, the spare-wheel hutch in a car that is supposed to be made from reinforced polypropylene in order to save weight.

second blend component, the PP in this case) are coated by a thin layer of the added compatibilizer. The latter prevents the direct contact between PET and PP and this suppresses the epitaxial as well as the nucleating effect of PET microfibrils on the crystallization, *i.e.*, transcrystalline layers cannot be formed. What is more, in an extended study on the same topic it was found that if the compatibilizer is added to the blend before drawing, the starting microspheres of the minor blend component coated with compatibilizer cannot coalesce in order to be transformed during the cold drawing into microfibrils [65].

In conclusion, the microindentation hardness study performed reveals conspicuous differences at the interphase boundary of blends of PS and natural rubber compatibilized with SBS. In the PS/SBS and PS/NR blends, the decrease of hardness through the phase boundary (50–100  $\mu\text{m}$  distance) occurs very rapidly when approaching the soft phase, showing a drastic fall of the initial hardness value. On the other hand, the compatibilized PS/NR/SBS blend exhibits a thinner phase boundary of about 25  $\mu\text{m}$ , showing a smoother decrease of the hardness. Thus, it is shown that the microhardness technique, particularly in combination with SEM, is a sensitive tool for the quantitative evaluation of the nature and quality of the interphase boundary in polymer blends.

### 13.5.2. *Microhardness on the interphase boundaries in polymers after double injection molding processing*

Earlier studies [66] have shown that microhardness may provide useful information about the correlation of processing parameters between, near and at the weld line or knit line, *i.e.*, the region where separated melt fronts reunite. In practice, *weld lines* occur in injection molding, *i.e.*, after a flow obstacle or, in the case of multiple gating, for melt streams of the same material or, in the case of two-component injection molding, for melt streams of different polymer materials [67]. In general, the presence of a weld line has an effect on the surface appearance and the mechanical properties of the molded parts [68].

The use of microhardness to characterize changes in the microstructure, molecular orientation, and micromechanical properties of injection-molded polymer materials has been the object of increasing interest [1,8]. In addition, it is known that process variables induce important changes in the microstructure and properties of the molded material. Hardness variations often occur in the surface and across the thickness of the molded samples. As a result, the mechanical properties can be controlled by processing variables such as melt and mold temperature, injection pressure, *etc.* [69].

Recently, a study reported [58] of the microindentation hardness measurements across the weld line arising when two opposite flow fronts are filling the cavity of a mold using two glassy polymers, polycarbonate (PC) and polystyrene. A large hardness difference between  $H$  measured away from the weld line and  $H$  measured at  $z = 0$  ( $H_{\text{min}}$ ) was found. For PC this difference was about 20 MPa (14%), while for PS it was larger than 50 MPa (~30%) [58]. The  $H$  measurement along the injection direction  $z$  for the PC and PS samples

containing a pigment for better visualization of the flow front was also performed [70], and the  $H_{\min}$  value defining the weld line was identified. Asymmetry of  $H$  values, between the sample side containing the pigment and the other side without pigment, was observed. For both polymers, the higher  $H$  values measured on the side containing the pigment show the hardening effect of the pigment within the polymer. Such an asymmetry contrasts with that when no pigment is used [58].

It seemed interesting to extend the above studies [58] to the two glassy polymers (PC and PS) processed using a two-component injection molding system. Specifically, the target was to examine the effect of the processing temperature on the  $H$ -value across the weld line arising when the two opposite flow fronts are filling the cavity of the mold [60]. In addition, for the sake of comparison, the measurements were carried out close to the edge and in the middle of the sample as shown schematically in Figure 13.7b.

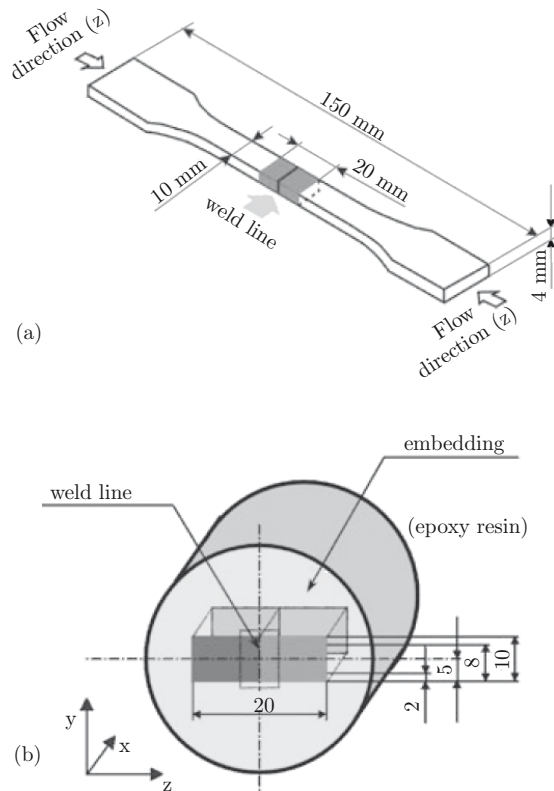


**Figure 13.7.** Schematic representation of a doubly injection-molded sample showing front weld line (a) and the measuring lines (at 2, 5, and 8 mm from the sample edge) parallel to the injection direction and across the weld line (b) [60]

The moldings were prepared in the form of ISO 3167 Type A tensile bars using a two-component injection-molding machine in which both melt streams (of the same material, though differently colored by 2 wt% of PS or PC color-batch, respectively) could be controlled independently (Figure 13.7a). The bars were molded using for PC melt temperatures  $T_m$  of 270°C and 300°C, respectively and a mold temperature (at the mold surfaces),  $T_w = 80^\circ\text{C}$ . In the case of PS, values of  $T_m = 230^\circ\text{C}$  and 270°C and of  $T_w = 50^\circ\text{C}$  were used. From the injection-molded tensile bars, the central part containing the weld line with a total length of 20 mm was cut. The sample was then embedded in an epoxy resin in order to enhance the sample fixing during subsequent measurements (Figure 13.7b,  $z$  is the flow direction).

Microhardness was measured across the weld line at the surface of each of the moldings. Special care was taken to make indentations with the diagonals parallel and perpendicular to the injection direction ( $z$ ), since the melt flow induced orientation may affect the diagonal sizes and thus the microhardness values too.

While Figure 13.7 presents the schematics of an injection-molded sample showing the shape of the melt front (containing a pigment) and the location of the measurements across the weld line, Figure 13.8 shows the optical micrograph of the surface of a PC sample after performing several indentations.

In contrast to previous measurements on the same systems [54], in which practically only one or two measurements characterized the deep decrease of

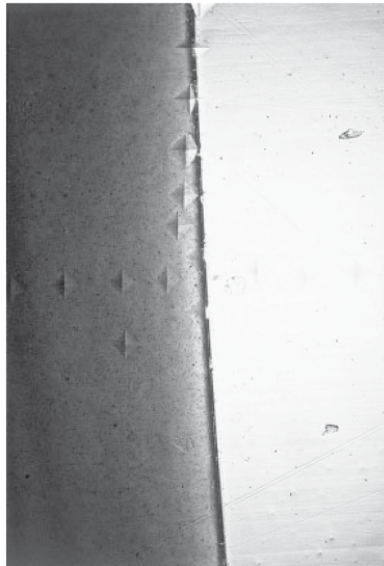


**Figure 13.8.** Optical micrograph of indentations at the surface of an injection-molded PC sample near the weld line area (left-hand side with pigment) [60]

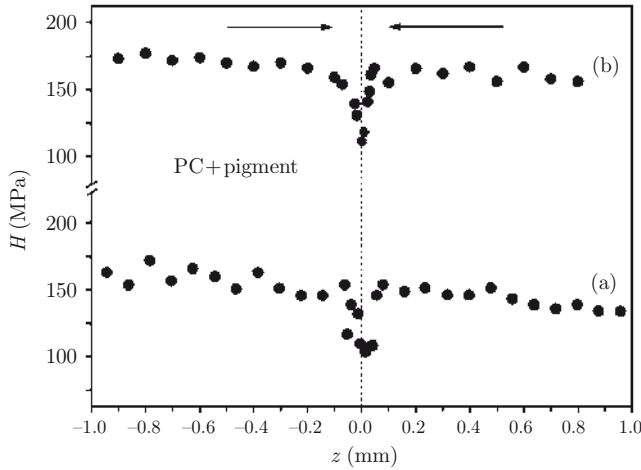


**Figure 13.9.** Microhardness,  $H$ , measured at the surface of the molding along the injection direction,  $z$ , for PC with melt temperature of 270°C. Arrows denote the direction of the two opposing fronts: measurements are performed along the injection direction (Figure 13.7) at a distance from the sample edge as follows: (a) – 2 mm and (b) – 5 mm. The left part of the sample contains a pigment. The right one does not contain the pigment [60]

$H$  on the weld line, in the present case the same line is defined by 5–10 indentations that makes the reported microhardness decrease more reliable.

Figure 13.9 illustrates the  $H$  variation on the surfaces of the molding along the injection direction,  $z$ , for the PC samples with a melt temperature of 230°C taken at 2 mm (Figure 13.9a) and 5 mm (Figure 13.9b) from the edge.

Results clearly show the gradual  $H$  decrease for both 2 and 5 mm measurements along the  $z$  direction, until a minimum value at  $z = 0$  is reached. Then, one observes a further increase of  $H$  when indenting away from  $z = 0$ . The symmetry of the hardness profile about  $z = 0$  is evident in both cases (Figures 13.9a and 13.9b). The weld line zone containing the  $H$  changes is defined in the PC case within a 0.10 mm region, which is much smaller than the previously reported one (1 mm) for the same polymers [58]. The observed difference in both cases for the same material obviously originates from the more reliable definition of the weld line due to the much larger number of experimental points in the present case as compared to the previous one [58]. The  $H$  value was determined within  $\Delta H/H \approx 0.5$ .

Most interesting is to note the large hardness difference found between  $H$  measured away from the weld line and  $H$  measured at  $z = 0$  ( $H_{\min}$ ). For PC this difference is about 50 MPa (~30%) for both measurements (Figures 13.9a and 13.9b). It should be noted that  $H$  measurements at a distance of 8 mm from the same sample edge (Figure 13.7) were also performed. The values obtained are the same as those measured at 2 mm distance from the edge (Figure 13.7) and therefore they are not plotted on the Figure 13.9 as well as on the subsequent one.